Research Article Vol. 36, No. 2 / February 2019 / Journal of the Optical Society of America A 245

Journal of the Optical Society of America A
OPTICS, IMAGE SCIENCE, AND VISION

Impact of sensor apodization on the tangential resolution in photoacoustic tomography

Pankaj Warbal,[1] Manojit Pramanik,[2,3] and Ratan K. Saha[1,4]

[1]Department of Applied Sciences, Indian Institute of Information Technology Allahabad, Jhalwa, Allahabad 211015, India
[2]School of Chemical and Biomedical Engineering, Nanyang Technological University, 62 Nanyang Drive, Singapore 637459, Singapore
[3]e-mail: manojit@ntu.edu.sg
[4]e-mail: ratank.saha@iiita.ac.in

Received 16 October 2018; revised 19 December 2018; accepted 20 December 2018; posted 21 December 2018 (Doc. ID 348464); published 25 January 2019

Photoacoustic tomographic (PAT) image reconstruction with apodized sensors is discussed. A Gaussian function was used to model axisymmetric apodization of sensors, and its full width at half-maximum (FWHM) was varied to investigate the role of apodization on the PAT image reconstruction. The well-known conventional delay-and-sum (CDAS) algorithm and recently developed modified delay-and-sum (MDAS) algorithm were implemented to generate reconstructed images. The performances of these algorithms were examined by comparing simulated images formed by these methods and that of ideal point detectors. Simulations in two dimensions were conducted using the k-Wave toolbox for three different phantoms. The results produced by the CDAS method are very close to that of ideal point detectors when the FWHM of the Gaussian function is small. The MDAS algorithm for flat sensors provides excellent results (comparable to that of point detectors) when the FWHM of the Gaussian profile is large. This study elucidates how sensor apodization affects PAT image reconstruction.

https://doi.org/10.1364/JOSAA.36.000245

1. INTRODUCTION

A tomographic imaging technique has been developed over the past two decades based on the photoacoustic (PA) effect [1–5]. When short pulses of a laser beam illuminate biological tissue, it undergoes thermoelastic expansion, and acoustic waves (known as PA waves) are generated. The PA signal is then acquired by detectors placed around the tissue surface. The sensor data are later used to map initial pressure rise or to reconstruct an image of the PA source distribution. This is known as PA tomography (PAT). PAT provides morphological information of the illuminated area and is found to be useful for breast imaging [6,7], sentinel lymph node imaging [8,9], small animal brain imaging [10,11], vasculature imaging [12], molecular imaging [13–15], and to study tumor angiogenesis [16,17]. In PAT, image reconstruction can be accomplished using analytical approaches such as back-projection or time reversal methods. It can also be performed exploiting model-based techniques. The back-projection method is simple and fast but delivers qualitative information of the tissue region only. On the other hand, more accurate quantitative information can be obtained utilizing the model-based procedures, but they are computationally expensive.

The scanning geometry in many PAT systems is chosen to be circular, i.e., the detectors are placed at various angular positions on the circumference of the circle to record the PA signals coming from the biological tissue [18]. A schematic diagram of a typical PAT scanning geometry is shown Fig. 1(a). These detectors are band-limited finite-aperture ultrasound transducers. It has been analytically shown in detail that these two factors related to the detector determine the resolutions of a PAT system [19]. Bandwidth dictates both the axial and tangential resolutions. Aperture size controls the tangential resolution. The axial and tangential resolutions are defined in Fig. 1(a). It has also been proved that the axial resolution remains spatially invariant, whereas the tangential resolution is space dependent. For example, tangential resolution for a given system is highest at the scanning center and deteriorates radially. In other words, the closer we go to the surface of the detector from the scanning center, the worse the tangential resolution.

Improvement of the tangential resolution can be done in two ways: either by reducing the transducer size so that it can accept signals from wider angles or by placing the detectors far away from the imaging region. The small-sized transducers have weaker sensitivity due to high thermal noise, whereas the other approach leads to a large scanning radius, which results in poor signal-to-noise ratio. The use of focused transducers (high numerical aperture) as virtual point detectors also improves tangential resolution [20]. A negative acoustic lens attached to a

planer transducer was also tried as a method to improve tangential resolution [21]. Although the acoustic lens increases the acceptance angle for the transducer, it also decreases its sensitivity (material dependent). Moreover, air gaps can also be formed between the lens and the transducer, leading to artifacts in the reconstructed image. There is also a provision for an inbuilt lens for a transducer (so there are no air gaps), but it would be custom made and hence expensive. Attempts have also been made to develop a method by modifying the reconstruction algorithm in order to enhance tangential resolution [22,23]. In the conventional delay-and-sum (CDAS) algorithm, large-aperture detectors are assumed as point detectors. The PA signals recorded by the detectors (incident PA waves undergo spatial averaging due to the large aperture) are back-projected from their centers to form an image. The modified delay-and-sum (MDAS) procedure involves the following steps: (i) it uniformly divides the PA signal detected by a transducer, (ii) it distributes those signals into different parts of that transducer, (iii) it executes the previous steps for each transducer, and (iv) it performs back-projection to reconstruct an image. It has been proved via simulation and experimental means that a more than threefold improvement of the tangential resolution can be achieved using the MDAS algorithm [22,23].

The aim of this work is to use simulations to study the performance of these algorithms when signals are detected by apodized transducers. Controlling the amplitude of normal velocity across the aperture of a transducer is known as the apodization [24,25]. It can be accomplished in many ways in the case of a single element transducer, such as: (i) by using a tapered electric field along the aperture, (ii) by dampening the beam on the face of the aperture, (iii) by altering the structure or geometry of the crystal, or (iv) by changing the phase in various regions of the aperture [24]. It is used in ultrasound imaging to lower the strengths of the side lobes and thus diminish artifacts to a great extent. As mentioned above, Xu and Wang [19] obtained analytical expressions of the point spread function as a function of bandwidth of the detection system and finite size of the recording aperture, assuming that the sensitivity of the detector remained constant throughout the aperture. In the current work, we investigate the effect of transducer apodization on PAT imaging, which has not been studied so far to our knowledge. Thus, the PA signals received by different parts of a detector were weighted by a Gaussian function and summed up to evaluate the resultant signal, emulating how a single element apodized ultrasound transducer would receive the PA signal. This signal was used for image formation using the CDAS and MDAS algorithms as shown in Figs. 1(b) and 1(c), respectively. Axisymmetric Gaussian functions with different full width at half-maximum (abbreviated as FWHM, and it is also mentioned as simply "width" in the text) values were used to generate various apodized conditions. Simulations in two dimensions were carried out in the k-Wave toolbox for three different phantoms. The aperture size of the sensors was also varied. It is shown that the CDAS algorithm with transducer apodization provides a more than threefold improvement. The MDAS protocol is found to be effective when apodization is weak.

The organization of the paper is as follows. The basic theoretical framework for PAT image reconstruction is detailed in Section 2. This section also describes the numerical method and reconstruction algorithms. Simulation results are elaborately presented in Section 3. Various aspects of our findings are discussed in Section 4. Section 4 also outlines the conclusions of this study.

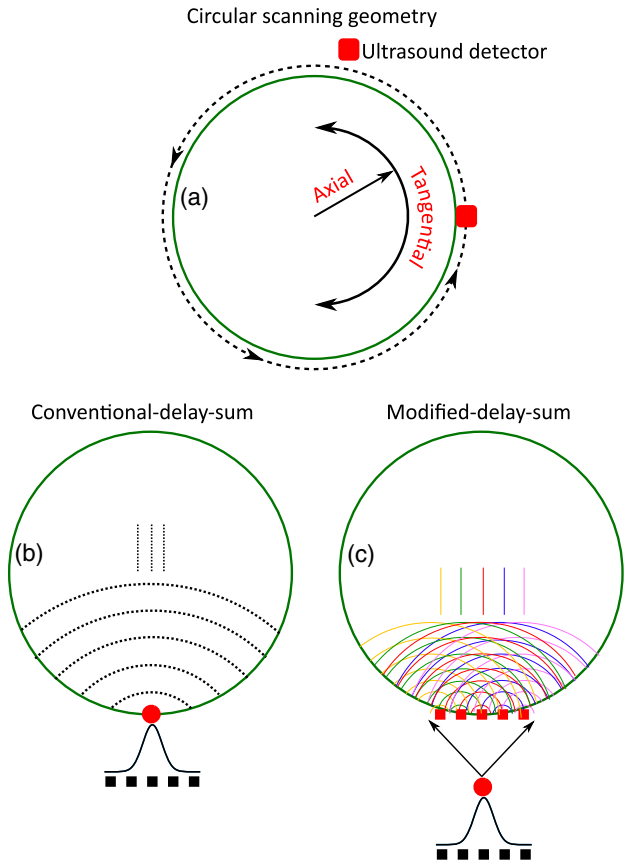

Fig. 1. (a) Scanning geometry showing the directions of axial and tangential resolutions. (b) Conventional delay-and-sum algorithm for a single transducer location. (c) Same as (b) but for the modified delay-and-sum algorithm.

2. MATERIALS AND METHODS

A. Basic Equations

The mathematical framework for PAT imaging is given in detail in previous publications [22,23]; however, relevant equations are presented here briefly for the sake of completeness. The PA pressure $p(\mathbf{r}, t)$ at a position $\mathbf{r}$ and time t developed in an acoustically homogeneous medium due to the absorption of electromagnetic radiation satisfies the following wave equation [26]:

$$\nabla^2 p(\mathbf{r}, t) - \frac{1}{v^2}\frac{\partial^2 p(\mathbf{r}, t)}{\partial t^2} = -\frac{\beta}{C_p}\frac{\partial H(\mathbf{r}, t)}{\partial t}, \tag{1}$$

where β is the isobaric thermal expansion coefficient, C_p is the specific heat, v is the speed of sound, and $H(\mathbf{r}, t)$ is a function that describes heating of the sample per unit time and volume. In practice, a $\delta(t)$ laser pulse is used to excite the sample, and if $A(\mathbf{r})$ is the spatial light energy absorption function,

then $H(\mathbf{r},t)$ can be decomposed as $H(\mathbf{r},t)=A(\mathbf{r})\delta(t)$. Equation (1) therefore becomes [1]

$$\nabla^2 p(\mathbf{r},t)-\frac{1}{v^2}\frac{\partial^2 p(\mathbf{r},t)}{\partial t^2}=-\frac{p_0(\mathbf{r})}{v^2}\frac{d\delta(t)}{dt}, \tag{2}$$

where $p_0(\mathbf{r})=\Gamma(\mathbf{r})A(\mathbf{r})$ is the initial pressure rise due to absorption of light. Here, $\Gamma(\mathbf{r})=\frac{\beta v^2}{C_p}$ is the Grüneisen parameter. The solution to Eq. (2) can be easily obtained in the frequency domain using Green's function approach. Therefore, by solving this forward problem, one can estimate PA pressure at a field point if the spatial profile of the initial pressure rise of the illuminated region is known.

In PAT, we essentially deal with an inverse problem. This means that one attempts to find initial pressure distribution $p_0(\mathbf{r})$ or absorption distribution $A(\mathbf{r})$ inside the imaging region from a set of data $p(\mathbf{r}_0,t)$ measured at $\mathbf{r}_0$. The exact analytical solutions for $A(\mathbf{r})$ utilizing Green's function approach can be found in the literature for planner, cylindrical, and spherical detection geometries [19]. The solutions are achieved by expanding Green's function in terms of appropriate functions for the corresponding geometries [19]. However, these Fourier domain reconstruction formulas are not straightforward to calculate because they involve multiple integration or series summations. The same group later proposed a simplified time domain reconstruction formula known as the universal back-projection algorithm, expressed as [27]

$$p_0^b(\mathbf{r})=\int_{\Omega_0} b\left(\mathbf{r}_0,t=\frac{|\mathbf{r}-\mathbf{r}_0|}{v}\right)\mathrm{d}\Omega_0/\Omega_0, \tag{3}$$

where

$$b(\mathbf{r}_0,t)=2p(\mathbf{r}_0,t)-2t\frac{\partial}{\partial t}p(\mathbf{r}_0,t) \tag{4}$$

is the back-projection term and

$$d\Omega_0=\frac{dS_0}{|\mathbf{r}-\mathbf{r}_0|^2}\left[\mathbf{n}_0\cdot\frac{(\mathbf{r}-\mathbf{r}_0)}{|\mathbf{r}-\mathbf{r}_0|}\right] \tag{5}$$

is the solid angle subtended by the detection element dS_0 at the reconstruction point $\mathbf{r}$; $\mathbf{n}_0$ is the unit vector normal to the measurement surface and Ω_0 is the total solid angle subtended by the recording area at $\mathbf{r}$. It is well known that for 2D, $\Omega_0=2\pi$ and for 3D, $\Omega_0=4\pi$.

The PA signals generated by an absorbing region are captured by detectors with finite aperture size placed at different angular positions in a typical PAT system. Therefore, output signal for a receiver can be written as

$$p'(\mathbf{r}_0,t)=\int p(\mathbf{r}_0',t)W(\mathbf{r}_0')\mathrm{d}^2\mathbf{r}_0', \tag{6}$$

where $W(\mathbf{r}_0')$ is the weighting factor. Equation (6) states that in general different parts of a large-aperture transducer may have different sensitivities, and thus the resultant signal has to be calculated by taking the weighted sum of impinging pressure waves. In this study, we assume that the sensitivity of the detector varies in a Gaussian manner with respect to the center, and therefore Eq. (6) reduces to

$$p'(\mathbf{r}_0,t)=\int p(\mathbf{r}_0',t)e^{-\frac{|\mathbf{r}_0'-\mathbf{r}_c'|^2}{2\sigma^2}}\mathrm{d}^2\mathbf{r}_0', \tag{7}$$

where σ is the standard deviation of the Gaussian apodization function and $\mathbf{r}_c'$ is the center of the transducer [24,25,28]. Equation (7) has been computed in this work to evaluate the resultant PA signal for large-aperture detector, and then the back-projection term has been evaluated.

B. Numerical Simulation

In this study, we considered three different numerical phantoms. The first phantom consisted of five point sources. The point sources were placed axially at 0, 2.4, 4.8, 7.2, and 9.6 mm, respectively, from the center of the image as shown in Fig. 2(a). This phantom allowed us to study how axial and tangential resolutions would depend upon sensor aperture size and apodization in PAT imaging. The second phantom was a variant of the Derenzo phantom, which contained a series of filled circles with increasing diameter [see Fig. 2(b)]. This would help to examine the effect of the size of the PA source on image reconstruction. It may be noted that blood happens to be the ideal medium for PA imaging because it contains hemoglobin, which acts as endogenous chromophore. Therefore, we designed a phantom that mimicked a blood vessel network as displayed in Fig. 2(c).

Each phantom was included as a binary image (strength is equal to 1 inside the source and 0 outside) within the numerical code to simulate the PA signals using the k-Wave toolbox in MATLAB. The corresponding computational setup is presented in Fig. 2(d). The computational region was discretized into 341×341 grid points with a resolution of 0.1 mm.

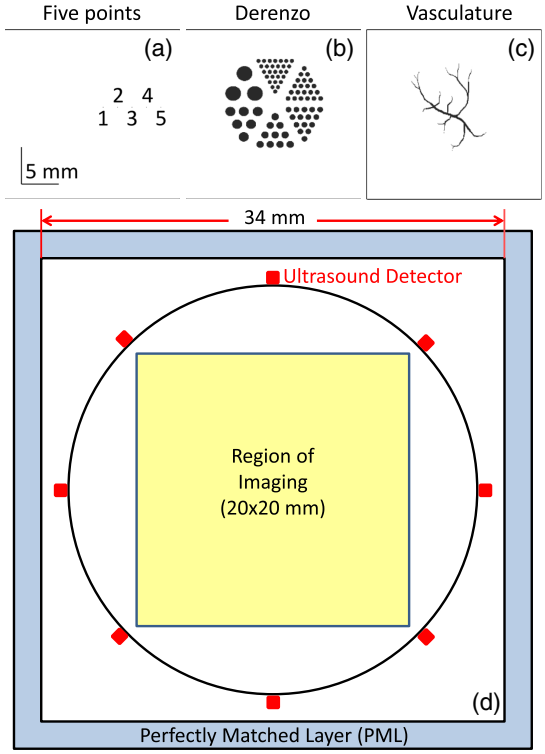

Fig. 2. (a) Five point sources phantom. (b) Derenzo phantom. (c) Vasculature phantom. Initial pressure for the white region is equal to 0, and for the black region it is considered as 1. (d) Illustration of the simulation geometry.

An absorbing layer of 2 mm width was placed at each boundary as shown in the figure. The imaging region of size 201 × 201 grid points was placed at the center of the computational domain. The density and speed of sound throughout the medium were chosen as 1000 kg/m^3 and 1500 m/s, respectively. The medium was assumed to be acoustically lossless. The imaging region was circularly surrounded by a number of detectors with 15 mm as the scanning radius to capture the PA signals. In this study, 200 detectors were positioned uniformly, covering an angle 0–2π. Flat detectors with 6 mm and 12 mm as the diameters were taken to investigate how aperture size and apodization would jointly affect the PAT resolution. The Gaussian function with widths $\sigma = 0.6, 2.0$, and 5.0 mm were used to model different apodization conditions. These numerical values were chosen phenomenologically. It might be noted that the detectors were basically line sensors, as the simulations were conducted in 2D. A finite size detector was broken into a number of points (51 points for 6 mm and 101 points for 12 mm). The nearest grid points for such points were determined, and time-dependent pressure fields were stored at those points for a sensor with 2.25 MHz as the center frequency and 70% bandwidth. A 40 dB noise level was also added. Sampling interval was 20 ns, and the PA pressure values at 1608 time points were saved for each sensor point.

C. Reconstruction Algorithms

As stated earlier, a large detector was broken into a number of points, and the PA signal at each point location was computed by running the forward model using the k-Wave toolbox. Then a Gaussian apodization function was used and generated a resultant PA signal from those signals [see Eq. (7)]. This step was repeated for all transducer positions. After that, the back-projection term was calculated for each detector [see Eq. (4)]. The second term in Eq. (4) was omitted for simplicity during computation. The resultant signals for all transducer locations were then back-projected and added for every pixel to generate a reconstructed image. This is the CDAS algorithm incorporating transducer apodization. It might be mentioned here that each detector was a part of a large detector and also a point sensor. Therefore, we did not include any factor for $d\Omega_0$ while calculating Eq. (3). The width of the Gaussian function was also varied to examine its effect on image reconstruction. In the MDAS algorithm, the resultant PA signal was redistributed equally into the same number of points, and after that, the CDAS method was followed. This means that no Gaussian weight was used while calculating signals for each of the point locations of a large detector. The algorithms are schematically described in Figs. 1(b) and 1(c), respectively. MATLAB codes were written to implement the back-projection algorithms for this work. All the simulations were executed in a personal computer with 64 bit OS, i5 processor, 3.50 GHz clock speed, and 12 GB RAM. Approximate run time was 2 min for each phantom.

To quantitatively determine the performance of the reconstruction algorithms under different apodization conditions, we have calculated the Pearson correlation coefficient (PCC), which is defined as

$$\mathrm{PCC} = \frac{\mathrm{COV}(x, x_r)}{\mathrm{STD}(x)\mathrm{STD}(x_r)}, \tag{8}$$

where x and x_r are the nominal and reconstructed initial pressure distributions, respectively. Here, STD indicates standard deviation and COV denotes covariance. The PCC's numerical value varies from −1 to 1. The higher the value of the PCC, the better the reconstruction.

3. SIMULATION RESULTS

Figure 3(a) displays the reconstructed image for the first phantom using 200 ideal point detectors uniformly located between 0 and 2π. The image is normalized by its maximum pixel value. The color bar shows the corresponding grayscale values. It can be seen that the point sources are well reproduced. However, each reconstructed point transforms into a blurred circle, which was also observed previously [22]. This distortion is expected because we have considered band-limited detectors. Enlarged images of the reconstructed points are presented in Figs. 3(a1)–3(a5), respectively, for better visualization of minute changes. The size and shape of the blobs in all these figures are identical. This confirms that axial and tangential resolutions in a reconstructed PAT image do not vary spatially when point detectors are used to record the signals.

Normalized PAT images generated using the CDAS algorithm are shown in Figs. 3(b)–3(d) for a flat sensor with 12 mm as the diameter and under different apodization conditions. In these cases, PA data were also collected at 200 angular locations. It is noted that the reconstruction is perfect [like in Fig. 3(a1)] when the source is situated at the scanning center. Nevertheless, a blob transforms into a thick arch for a point source situated away from the center. Further, arch length increases as the radial distance of the source from the center increases. The rate of increase of arch length is minimum for $\sigma = 0.6$ mm [see Fig. 3(b)]. It grows as the apodization effect decreases or σ increases and reaches to its maximum for $\sigma =$ 5.0 mm [see Fig. 3(d)]. The simulated images for the MDAS technique are presented in Figs. 3(e)–3(g). Interestingly, the completely opposite trend compared to Figs. 3(b)–3(g) can be observed. Figure 3(e) illustrates that the MDAS algorithm cannot recover initial pressure values when apodization is strong [i.e., $\sigma = 0.6$ mm]. However, it provides great improvement when the width of the Gaussian apodization function is large [Figs. 3(f)–3(g)]. The arch lengths for the farthest point source have been reduced significantly [see Figs. 3(f5) and 3(g5)] in comparison to Fig. 3(e5). The reconstructed images for 6 mm diameter sensor exhibit similar trends, and that is why those figures have not been included here.

Quantitative values of the tangential resolution are further plotted in Fig. 4 for different recording configurations. The same plot for a point detector is also presented in each figure for ready reference. It is evident from this figure that the tangential resolution deteriorates axially for all conditions. However, for the CDAS algorithm, it is improved approximately by a factor of 2 for the 6 mm case when σ varied from 5.0 to 0.6 mm for the farthest point source as shown in Fig. 4(a). Under the same conditions, improvement can be found to be nearly 3.5 times for the 12 mm case [see Fig. 4(c)]. The MDAS method demonstrates the completely reversed trend, as stated earlier. The enhancements of the tangential resolution for this algorithm are computed to be 1.3 and 3 times for those detectors, respectively,

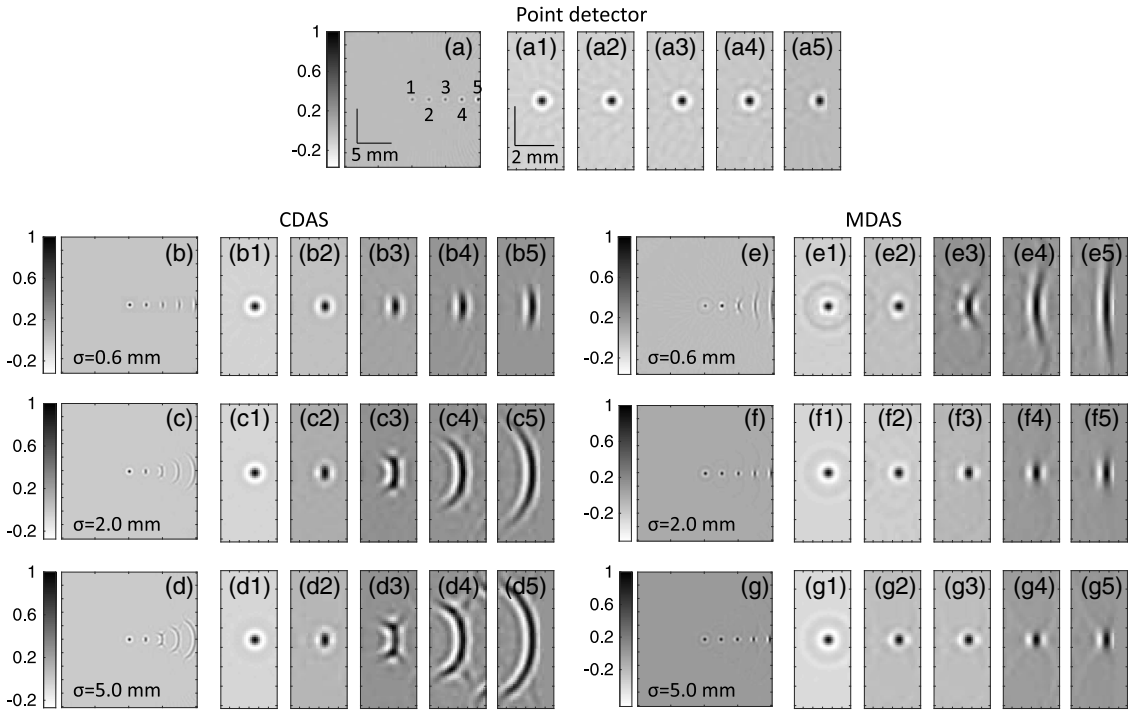

Fig. 3. (a) Reconstructed image of point sources when 200 ideal point detectors were used to collect the PA signals. A color bar is attached with the image to display the numerical values for graylevels. (a1)–(a5) Magnified images of those point sources. (b)–(d) Reconstructed images using the CDAS algorithm for the same phantom with 12 mm diameter sensor (flat) and $\sigma = 0.6$, 2.0, and 5.0 mm, respectively. The PA signals were captured from 200 angular positions. The corresponding zoomed images are also shown. (e)–(g) Similar images formed employing the MDAS algorithm for the same apodization conditions.

when σ is altered from 0.6 to 5.0 mm for the same source position [see Figs. 4(b) and 4(c)].

Normalized reconstructed images of the Derenzo and vasculature phantoms are shown in Figs. 5 and 6, respectively, under certain apodization conditions. Accurate reconstruction is possible using point detectors as shown in Fig. 5(a). It may be noted that each large circle appears like a ring. This may be attributed to the fact that we do not have low-frequency

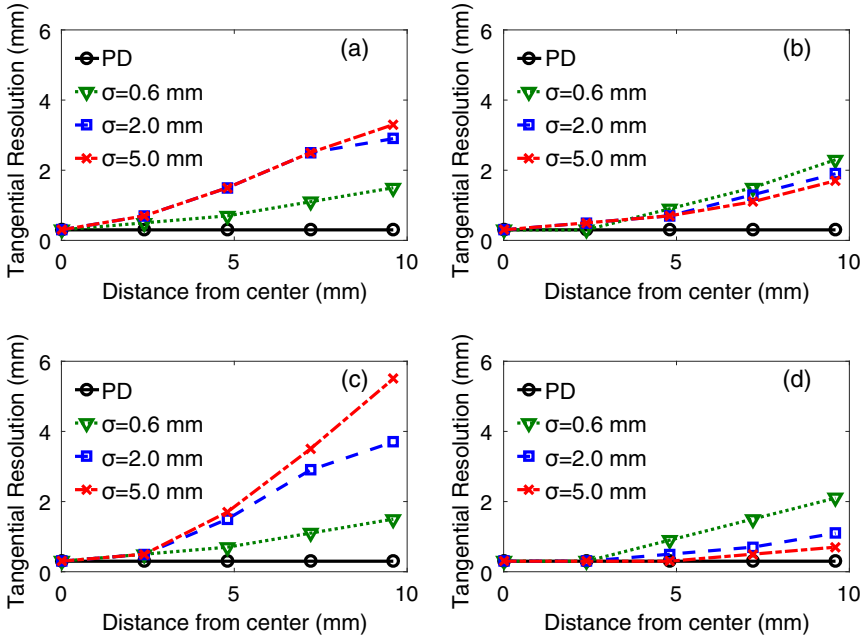

Fig. 4. Plots of tangential resolution as a function of distance of the source from the imaging center for flat sensors at different apodization conditions; (a) and (b) for CDAS and MDAS algorithms, respectively, for a 6 mm sensor. (c) and (d) Same as (a) and (b), respectively, but for a 12 mm sensor. PD means ideal point detector.

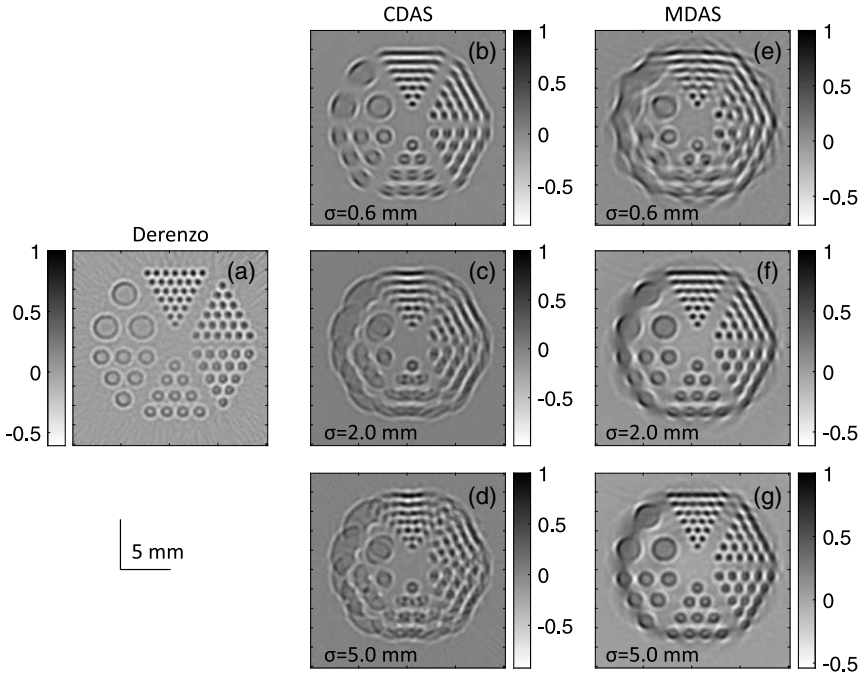

Fig. 5. (a) Reconstructed image of Derenzo phantom using ideal point detectors. (b)–(d) Reconstructed images generated by the CDAS algorithm for a 12 mm sensor (flat) with $\sigma = 0.6, 2.0$, and 5.0 mm, respectively. (e)–(g) Same as (b)–(d), respectively, but for the MDAS algorithm.

components as we have used transducers with finite bandwidth. The conventional algorithm works best when σ is small. For instance, circular objects far away from the scanning center have been faithfully reconstructed [see Fig. 5(b)]. However, this method performs poorly when σ becomes large [see Fig. 5(d)]. On the contrary, the modified technique produces its best quality images for weak apodization. For example, it can be seen from Fig. 5(g) that circular shapes are almost exactly recovered, even for the distant objects. Further, the quality of the reconstructed image degrades as σ decreases. Similar observations can be made from Fig. 6. Numerical values of the Pearson correlation coefficient are provided in Table 1 to assess the performance of

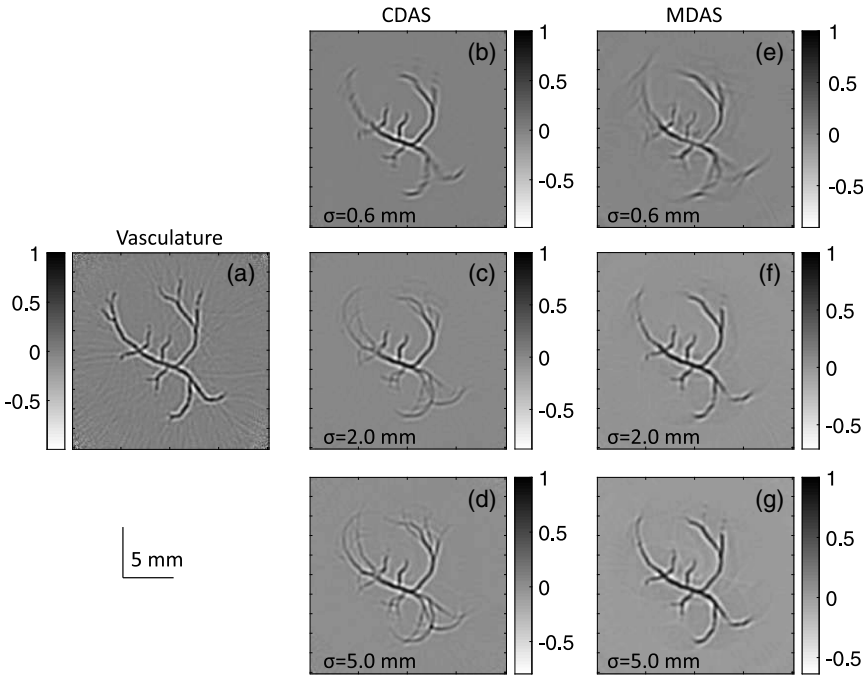

Fig. 6. (a) Reconstructed image of vasculature phantom using ideal point detectors. (b)–(d) Reconstructed images are created by the CDAS algorithm for a 12 mm sensor (flat) with $\sigma = 0.6, 2.0$, and 5.0 mm, respectively. (e)–(g) Same as (b)–(d), respectively, but for the MDAS algorithm.

Table 1. Comparison between Actual and Reconstructed Images Using the Pearson Correlation Coefficient for Flat Sensors[a]

Aperture Diameter	σ Values	Five Points		Derenzo		Vasculature	
		CDAS	MDAS	CDAS	MDAS	CDAS	MDAS
PD		0.29	0.29	0.61	0.61	0.62	0.62
6 mm	0.6 mm	0.26	0.20	0.55	0.45	0.59	0.58
	2.0 mm	0.20	0.23	0.40	0.49	0.41	0.59
	5.0 mm	0.19	0.23	0.38	0.49	0.38	0.58
12 mm	0.6 mm	0.26	0.19	0.55	0.39	0.59	0.51
	2.0 mm	0.19	0.27	0.40	0.61	0.41	0.72
	5.0 mm	0.17	0.28	0.36	0.69	0.35	0.74

[a]Here, PD indicates point detector.

these algorithms. It is clear from Table 1 that the CDAS procedure can reproduce initial pressure distribution well when the width of the Gaussian function is narrow; nevertheless, the accuracy of the MDAS algorithm improves with increasing width.

4. DISCUSSION AND CONCLUSIONS

Single element transducers with finite aperture size have been almost exclusively used in PAT imaging works. This is because such transducers are easily available in the market and provide good signal-to-noise ratio. However, the PA waves impinging on the surface of a large detector become spatially averaged, and thus the high-frequency components are filtered out. As a result, reconstructed images become blurred. In this simulation study, we used apodized transducers. A Gaussian function was used to model transducer apodization, and its width was varied to examine the effect of apodization on PAT imaging. The PA signals recorded by apodized sensors were utilized for image reconstruction. A large detector with small σ (i.e., the central part of the sensor would be most sensitive and the region away from the center would be less sensitive) effectively acted like a point detector and hence provided fairly good PAT images.

The CDAS algorithm was applied for image reconstruction. It is a trivial and fast method. It was found that this method was able to recover initial pressure very close to that of ideal point detectors when the width of the Gaussian function was narrow ($\sigma = 0.6$ mm). An approximately 3.5-fold enhancement of the tangential resolution has been computed for a 12 mm detector [see Fig. 3(b5) with respect to Figs. 3(d5) and 4(c)]. Another simple protocol called the MDAS algorithm was also employed in this study for image formation. The major advantage of this method is that it can be implemented at the software level. This study also shows that 3 times improvement of the tangential resolution is possible by this algorithm for flat sensors with 12 mm diameter with large σ [see Fig. 3(g5) with respect to Figs. 3(e5) and 4(d)]. These values are consistent with the previous simulation and experimental findings [22,23]. This algorithm redistributed the PA signal (captured by a large detector) equally among many small segments lying on the surface of the detector. This step introduced small phase differences between signals (coming from different detector segments) while meeting at a pixel location, and the resultant signal (due to interference) might have mimicked the original emitted signal in a better manner than that of the CDAS. Consequently, improved reconstruction was achieved for large σ for which spatial averaging was significant. However, spatial averaging was less for small σ, and therefore reconstruction was poor. The MDAS algorithm took a longer time to execute (≈80 s) than the CDAS algorithm (≈1 s) because more elements were taken into account during reconstruction using back-projection. For example, 200 angular positions were considered in the first algorithm, but it was 200 × 101 in the second algorithm when a sensor was divided into 101 elements.

It is important to note that the resultant PA signal measured by a detector in this work was uniformly distributed at the point locations on the surface of the detector in the MDAS procedure, and reconstruction was performed accordingly. In addition, we also used the Gaussian weighting coefficients while calculating time series pressure data associated with those point locations and studied how it would affect image reconstruction. The simulation results (not shown here) reveal that if this procedure is adapted, then the MDAS algorithm provides results comparable to that of the CDAS, even in the case of strong apodization. The computed PCC values for both the algorithms become comparable for all phantoms at $\sigma = 0.6$ mm. Therefore, the MDAS algorithm in both the cases (strong and weak apodizations) works faithfully and proves to be a robust algorithm if the Gaussian weighting is incorporated in both directions (signal acquisition and back-projection) for apodized detectors.

The Gaussian apodization has been extensively used in ultrasound imaging, since it can suppress side lobes, removing artifacts substantially [24,25,28]. A similar operation may be carried out in PAT to reduce image artifacts. It may be emphasized here that implementation of Gaussian apodization for single element transducers is in general challenging because it has to be performed during transducer construction. It may also be speculated that the sensitivity of the transducer may be reduced greatly (particularly when the FWHM of the Gaussian function is small) due to apodization, which will limit its use in practice. It may be relatively simple for array transducers because it may be implemented at the software level if radio frequency signals are accessible for different channels, and improved image formation may be possible. Effort has been made recently in this direction as well [29]. Therefore, in the future, we aspire to design further simulation and experimental studies to verify our findings.

Further, both the CDAS and MDAS methods essentially employ the back-projection algorithm to reconstruct an image of the initial pressure distribution. The back-projection method is an analytical approach and is computationally efficient but lacks the ability to facilitate quantitative information of the imaging region as discussed earlier. Therefore, efforts may be directed in the future to implement model-based reconstruction algorithms to better estimate the initial pressure rise [30–32]. These techniques are in general computationally expensive because they deal with a large matrix known as the system matrix, which includes properties of the medium, wave propagation, and detectors. They work iteratively and obtain

the best solution via implementing the Tikhonov regularization scheme.

In conclusion, the effect of the Gaussian apodization of an ultrasound detector on PAT image reconstruction has been studied. Single element flat transducers were considered, and simulations were conducted using the k-Wave toolbox. Three different phantoms, namely, point sources, Derenzo, and vasculature were used in this study. Extensively used CDAS and recently developed MDAS protocols were implemented for the PAT image reconstruction, and those results were compared with those of the ideal point detectors. It is found that the CDAS algorithm provides results very close to those of the ideal point detectors if the width of the Gaussian function is narrow. The MDAS method facilitates excellent reconstruction when the transducer surface is flat and the width of the Gaussian function is wide. Therefore, the CDAS technique may be preferred for flat sensors in practice if the apodization is strong, and the MDAS algorithm may be applied if apodization is weak.

Acknowledgment. The authors thank Anuj Kaushik and Deepak Sonker for stimulating discussion.

REFERENCES

1. L. V. Wang, *Photoacoustic Imaging and Spectroscopy* (CRC Press, 2009), Chap. 4, pp. 37–46.
2. L. Lin, P. Hu, J. Shi, C. M. Appleton, K. Maslov, L. Li, R. Zhang, and L. V. Wang, "Single-breath-hold photoacoustic computed tomography of the breast," Nat. Commun. **9**, 2352 (2018).
3. L. Li, L. Zhu, C. Ma, L. Lin, J. Yao, L. Wang, K. Maslov, R. Zhang, W. Chen, J. Shi, and L. V. Wang, "Single-impulse panoramic photoacoustic computed tomography of small-animal whole-body dynamics at high spatiotemporal resolution," Nat. Biomed. Eng. **1**, 0071 (2017).
4. P. K. Upputuri and M. Pramanik, "Recent advances toward preclinical and clinical translation of photoacoustic tomography: a review," J. Biomed. Opt. **22**, 041006 (2017).
5. L. V. Wang and J. Yao, "A practical guide to photoacoustic tomography in the life sciences," Nat. Methods **13**, 627–638 (2016).
6. E. Fakhrejahani, M. Torii, T. Kitai, S. Kanao, Y. Asao, Y. Hashizume, Y. Mikami, I. Yamaga, M. Kataoka, T. Sugie, M. Takada, H. Haga, K. Togashi, T. Shiina, and M. Toi, "Clinical report on the first prototype of a photoacoustic tomography system with dual illumination for breast cancer imaging," PloS One **10**, e0139113 (2015).
7. I. Yamaga, N. Kawaguchi-Sakita, Y. Asao, Y. Matsumoto, A. Yoshikawa, T. Fukui, M. Takada, M. Kataoka, M. Kawashima, E. Fakhrejahani, S. Kanao, Y. Nakayama, M. Tokiwa, M. Torii, T. Yagi, T. Sakurai, H. Haga, K. Togashi, T. Shiina, and M. Toi, "Vascular branching point counts using photoacoustic imaging in the superficial layer of the breast: a potential biomarker for breast cancer," Photoacoustics **11**, 6–13 (2018).
8. K. Sivasubramanian, V. Periyasamy, and M. Pramanik, "Non-invasive sentinel lymph node mapping and needle guidance using clinical handheld photoacoustic imaging system in small animal," J. Biophoton. **11**, e201700061 (2018).
9. H. Kim and J. H. Chang, "Multimodal photoacoustic imaging as a tool for sentinel lymph node identification and biopsy guidance," Biomed. Eng. Lett. **8**, 183–191 (2018).
10. J. Tang, J. E. Coleman, X. Dai, and H. Jiang, "Wearable 3-D photoacoustic tomography for functional brain imaging in behaving rats," Sci. Rep. **6**, 25470 (2016).
11. P. K. Upputuri and M. Pramanik, "Dynamic in vivo imaging of small animal brain using pulsed laser diode-based photoacoustic tomography system," J. Biomed. Opt. **22**, 1–4 (2017).
12. K. Jansen, G. van Sofest, and A. F. W. van der Steen, "Intravascular photoaocustic imaging: a new tool for vulnerable plaque identification," Ultrasound Med. Biol. **40**, 1037–1048 (2014).
13. V. Ntziachristos, "Going deeper than microscopy: the optical imaging frontier in biology," Nat. Methods **7**, 603–614 (2010).
14. J. Weber, P. C. Beard, and S. E. Bohndiek, "Contrast agents for molecular photoacoustic imaging," Nat. Methods **13**, 639–650 (2016).
15. Y. Liu, L. Nie, and X. Chen, "Photoacoustic molecular imaging: from multiscale biomedical applications towards early-stage theranostics," Trends Biotechnol. **34**, 420–433 (2016).
16. K. Okumura, K. Yoshida, K. Yoshioka, S. Aki, N. Yoneda, D. Inoue, A. Kitao, T. Ogi, K. Kozaka, T. Minami, W. Koda, S. Kobayashi, Y. Takuwa, and T. Gabata, "Photoacoustic imaging of tumour vascular permeability with indocyanine green in a mouse model," Eur. Radiol. Exp. **2**, 5 (2018).
17. S. Nandy, A. Mostafa, I. S. Hagemann, M. A. Powell, E. Amidi, K. Robinson, D. G. Mutch, C. Siegel, and Q. Zhu, "Evaluation of ovarian cancer: initial application of coregistered photoacoustic tomography and US," Radiology **289**, 740–747 (2018).
18. S. K. Kalva, P. K. Upputuri, and M. Pramanik, "High-speed, low-cost, pulsed-laser-diode-based second-generation desktop photoacoustic tomography system," Opt. Lett. **44**, 81–84 (2019).
19. M. Xu and L. V. Wang, "Analytic explanation of spatial resolution related to bandwidth and detector aperture size in thermoacoustic or photoacoustic reconstruction," Phys. Rev. E **67**, 056605 (2003).
20. C. Li and L. V. Wang, "High-numerical-aperture-based virtual point detectors for photoacoustic tomography," Appl. Phys. Lett. **93**, 033902 (2008).
21. M. Pramanik, G. Ku, and L. V. Wang, "Tangential resolution improvement in thermoacoustic and photoacoustic tomography using a negative lens," J. Biomed. Opt. **14**, 024028 (2009).
22. M. Pramanik, "Improving tangential resolution with a modified delay-and-sum reconstruction algorithm in photoacoustic and thermoacoustic tomography," J. Opt. Soc. Am. A **31**, 621–627 (2014).
23. S. K. Kalva and M. Pramanik, "Experimental validation of tangential resolution improvement in photoacoustic tomography using modified delay-and-sum reconstruction algorithm," J. Biomed. Opt. **21**, 086011 (2016).
24. T. L. Szabo, *Diagnostic Ultrasound Imaging: Inside Out* (Academic, 2004), Chap. 6, pp. 137–170.
25. R. S. C. Cobbold, *Foundations of Biomedical Ultrasound* (Oxford University, 2007), Chap. 3, pp. 135–226.
26. G. J. Diebold, T. Sun, and M. I. Khan, "Photoacoustic monopole radiation in one, two and three dimensions," Phys. Rev. Lett. **67**, 3384–3387 (1991).
27. M. Xu and L. V. Wang, "Universal back-projection algorithm for photoacoustic computed tomography," Phys. Rev. E **71**, 016706 (2005).
28. R. Zemp and M. F. Insana, "Imaging with unfocused regions of focused ultrasound beams," J. Acoust. Soc. Am. **121**, 1491–1498 (2007).
29. J. Xiao, X. Luo, K. Peng, and B. Wang, "Improved back-projection method for circular-scanning-based photoacoustic tomography with improved tangential resolution," Appl. Opt. **56**, 8983–8990 (2017).
30. X. L. Dean-Ben, V. Ntziachristos, and D. Razansky, "Acceleration of optoacoustic model-based reconstruction using angular image discretization," IEEE Trans. Med. Imaging **31**, 1154–1162 (2012).
31. K. Wang, R. Su, A. A. Oraevsky, and M. A. Anastasio, "Investigation of iterative image reconstruction in three-dimensional optoacoustic tomography," Phys. Med. Biol. **57**, 5399–5423 (2012).
32. C. B. Shaw, J. Prakash, M. Pramanik, and P. K. Yalavarthy, "Least squares QR-based decomposition provides an efficient way of computing optimal regularization parameter in photoacoustic tomography," J. Biomed. Opt. **18**, 080501 (2013).